Simultaneous measurements of near-surface CO_2 and NO_2 to monitor the fossil-fuel combustion-derived CO_2 in the Greater Tokyo Area

Hitoshi Irie[1], Masataka Nomoto[1,2], Yoshikazu Kamiya[1,3], and Yukio Terao[4]

[1]Center for Environmental Remote Sensing, Chiba University, 1-33 Yayoicho, Inage-ku, Chiba 263-8522, Japan
[2]Ministry of Education, Culture, Sports, Science and Technology (MEXT), 3-2-2 Kasumigaseki, Chiyoda-ku, Tokyo 100-8959, Japan
[3]Chiba Prefectural Kisarazu High School, 4-1-1 Bunkyo, Kisarazu, Chiba 292-0804, Japan
[4]National Institute for Environmental Studies, 16-2 Onogawa, Tsukuba, Ibaraki 305-8506, Japan

Correspondence to: Hitoshi Irie (hitoshi.irie@chiba-u.jp)

Abstract. Year-round continuous measurements of near-surface carbon dioxide (CO_2) concentrations using in-situ trace gas analyzers were conducted simultaneously with nitrogen dioxide (NO_2) measurements by International Air Quality and SKY Research Remote Sensing Network (A-SKY) Multi-Axis Differential Optical Absorption Spectroscopy (MAX-DOAS) at Chiba (35.625°N, 140.104°E, 60 m above sea level), located within the Greater Tokyo Area, Japan, during 2024. These simultaneous measurements revealed that CO_2 concentrations were low on days when near-surface NO_2 concentrations were markedly reduced. Furthermore, the CO_2 enhancement relative to the baseline concentration determined based on such low-NO_2-concentration days ($[\Delta CO_2]_N$) was positively correlated with NO_2 and black carbon concentrations. This finding indicates that $[\Delta CO_2]_N$ is useful in observing the increase in fossil-fuel combustion-derived CO_2 within the Greater Tokyo Area. By employing this relatively simple method, CO_2 concentrations in megacities such as the Grater Tokyo Area can be monitored with high accuracy and precision, contributing to more effective emission mitigation strategies.

1 Introduction

The escalating climate crisis underscores the urgent need for precise monitoring of greenhouse gas emissions, particularly carbon dioxide (CO_2), which remains the dominant anthropogenic driver of global warming (e.g., IPCC, 2021). Megacities - urban agglomerations with populations exceeding ten million - are disproportionately responsible for global CO_2 emissions due to concentrated energy consumption, transportation, and industrial activity. Establishing robust monitoring frameworks in megacities is thus essential to bridge local action with global climate goals, ensuring that mitigation strategies are evidence-based, transparent, and effective. Effective mitigation of fossil-fuel CO_2 emissions requires continuous monitoring of atmospheric CO_2 concentrations. However, globally, only a limited number of megacity sites conduct continuous measurements of CO_2 concentrations near the surface (e.g., Li et al., 2026).

The Greater Tokyo Area, which is sometimes conventionally referred to as the Tokyo megacity, is one of the world's largest metropolitan areas, with a population exceeding 37 million as of 2018 (UNPD, 2018). The Greater Tokyo Area comprises Tokyo and its surrounding major cities, including Yokohama, Kawasaki, Saitama, and Chiba, along with their connected suburban districts. The primary sources of anthropogenic CO_2 emissions in Tokyo are power generation, automobile transportation, and industry (Long and Yoshida, 2018). Large point sources, such as power plants and steelworks, are located along the Tokyo Bay Area. In residential areas, fossil fuel-related CO_2 emissions arise from household gas consumption and traffic exhaust (Hirano et al., 2015). Sugawara et al. (2021) investigated anthropogenic CO_2 emission changes in an urban area of Tokyo during the COVID-19 pandemic and found that the CO_2 emissions decreased by 20% during the COVID-19 state of emergency compared to the same period during the past few years, mainly due to a decrease in car traffic. On the other hand, Shirai et al. (2012) analyzed aircraft CO_2 data over the Tokyo metropolitan region and found strong influences of

fossil fuel CO_2 originating from the Asian continent. Therefore, it is necessary to account for the significant contribution from the Asian continent, to evaluate or estimate emissions from the Greater Tokyo Area.

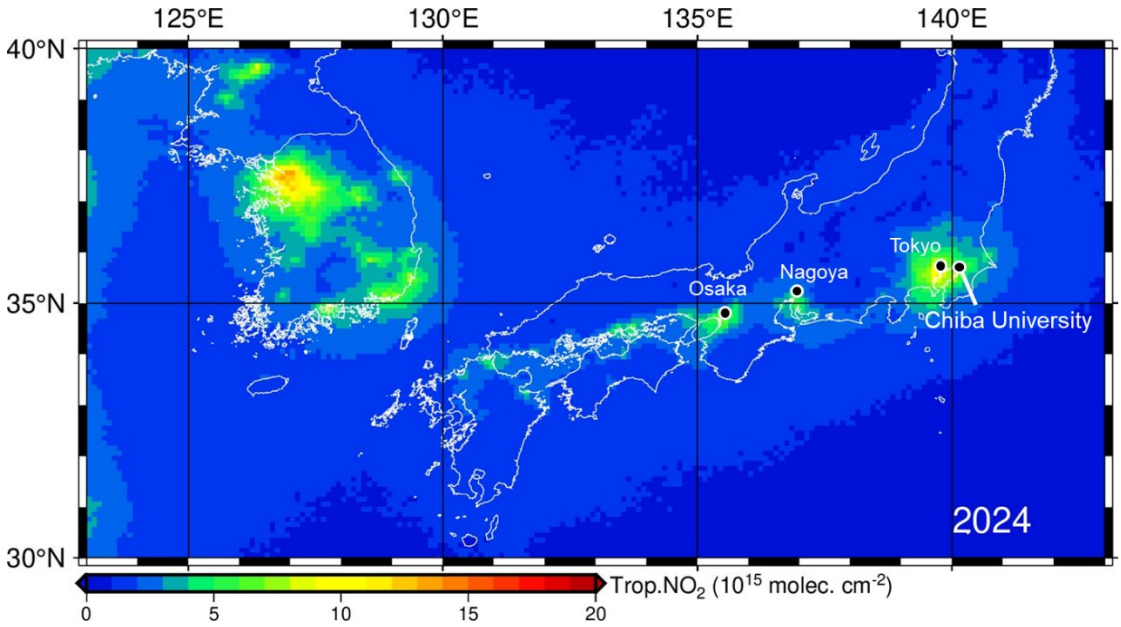

Figure 1: Location of Chiba University. Observations were conducted at the Chiba University Atmospheric Environment Observation Supersite, located on the Nishi-Chiba campus of Chiba University. The colors show the annual mean tropospheric NO_2 column concentration for 2024, retrieved from the Tropospheric Ozone Monitoring Instrument (TROPOMI) aboard Sentinel-5 Precursor (S5P) satellite (Verhoelst et al., 2021).

To constrain anthropogenic emissions of CO_2 from the Tokyo Bay Area, Pisso et al. (2019) employed a Lagrangian inverse model together with data from in-situ aircraft CO_2 observations by the Comprehensive Observation Network for TRace gases by AIrLiner (CONTRAIL), the Tsukuba tall tower of the Meteorological Research Institute (MRI) of the Japan Meteorological Agency, and surface sites from the World Data Center for Greenhouse Gases (WDCGG). As one of their conclusions, the challenges in estimating regional CO_2 fluxes from atmospheric observations were highlighted. Bisht et al. (2025) performed regional model simulations (WRF-GHG) with an improved resolution of 1×1 km^2 and found that point-source CO_2 emission and vertical distributions of CO_2 were better captured and represented. Yamada et al. (2025) conducted global high-resolution simulations of atmospheric CO_2 using flux data derived from global inverse analysis. Their simulations reproduced CO_2 variations at remote sites around Japan. Application of tagged tracers in the simulations revealed that variations in CO_2 concentrations at approximately 250 m above ground level from the Tokyo Skytree (35.71°N, 139.81°E) strongly depend on fluxes from the southwestern part of Tokyo, including the western Tokyo Bay Area where large power plants are located. Based on the results, Yamada et al. (2025) argued the necessity of CO_2 observations that can capture emissions from the east coast of Tokyo Bay Area.

Here, the present study focuses on the Chiba University Atmospheric Environment Observation Supersite (35.625°N, 140.104°E, 60 m above sea level) (Fig. 1), which is a key site in the international observation networks; International Air Quality and Sky Research Remote Sensing (A-SKY) network (e.g., Irie et al., 2021; Mizobuchi et al., 2025) and skyradiometer network (SKYNET) (e.g., Nakajima et al., 2020; Irie et al., 2022). Chiba is one of the key cities consisting of the Grater Tokyo Area, being located east of Tokyo, and lying downstream of major sources of air pollution (Fig. 1). From the satellite-retrieved tropospheric nitrogen dioxide (NO_2) data in Fig. 1, it is also evident that the Greater Tokyo Area is isolated from other major urban areas such as Nagoya and Osaka. At this important site, we conducted year-round continuous measurements of near-surface CO_2 concentrations using in-situ trace gas analyzers and ground-based remote sensing using the A-SKY Multi-Axis Differential Optical Absorption Spectroscopy (A-SKY/MAX-DOAS). From these

simultaneous measurements, an attempt was made to clarify the usefulness of simultaneous measurements of CO_2 and NO_2 measurement for simple and accurate monitoring of fossil-fuel combustion-derived CO_2 concentrations in the Greater Tokyo Area.

2 Observations

In the Chiba University Atmospheric Environment Observation Supersite, which is located east of Tokyo (Fig. 1), we conducted year-round continuous measurements of near-surface CO_2 concentrations using two different in-situ trace gas analyzer instruments in 2024. One is the LI-7810 trace gas analyzer (LI-COR, Inc.), which employs a high-precision single-frequency laser and uses Optical Feedback–Cavity Enhanced Absorption Spectroscopy (OF-CEAS) - a technique that combines Cavity-Enhanced Absorption Spectroscopy (CEAS) with Optical Feedback (OF) from a V-shaped optical cavity (Morville et al., 2014; Romanini et al., 2014). While the LI-7810 is optimized for precise methane (CH_4) measurements, it also provides concurrent measurements of CO_2 and water vapor (H_2O). Since the LI-7810 detects inherently weak CO_2 absorption signals that overlap with those of H_2O, the occurrence of drift, including H_2O-related interference, is anticipated. It should be noted that the LI-7810 outputs CO_2 concentration data for dry air. The other is the G4301 Cavity Ring-Down Spectrometer analyzer (Picarro, Inc.). On the rooftop of the same building, at 60 m above sea level, these two trace gas analyzers were operated simultaneously, each using its own inlet to conduct measurements independently. Measurements using the G4301 were calibrated regularly using three working standard gases that were further calibrated against the National Institute for Environmental Studies (NIES) CO_2 standard scale (Machida et al., 2011). Air samples for the G4301 were dehumidified by passing through a Nafion dryer. On the other hand, the observations using the LI-7810 were conducted without performing regular calibrations and without dehumidifying the sampled air. This approach was adopted to explore whether useful automated long-term measurements could be achieved with lower effort.

Simultaneously with the trace gas analyzers, we conducted measurements using the MAX-DOAS technique. Its principle is based on the DOAS method (e.g., Platt and Stutz, 2008), which derives trace gas concentrations using Lambert–Beer's law by exploiting the characteristic absorption spectral structures of target species contained in hyperspectral measurements with high wavelength resolution. The measured hyperspectra include not only absorption features of trace gases but also influences from Rayleigh and Mie scattering. These lower-frequency (smooth wavelength-dependent) structures are approximated and removed using polynomials. This enables the identification of absorptions as weak as 0.1% and allows highly precise retrieval of trace gas concentrations.

MAX-DOAS is a passive DOAS technique enhanced with multiple low-elevation angle measurements. Despite its relatively simple instrumentation, MAX-DOAS achieves precise retrievals by combining hyperspectral measurements at multiple elevation angles with high-accuracy wavelength calibration using Fraunhofer lines, radiative transfer modeling that accounts for atmospheric sphericity, and nonlinear inversion solved via the Levenberg–Marquardt method based on Bayes' theorem (e.g., Irie et al., 2011). This enables simultaneous retrieval of vertical distribution information of aerosols and trace gases in the lower troposphere.

At Chiba, four A-SKY/MAX-DOAS systems were operated simultaneously, each directed toward a different azimuth angle: north (13°W), west (95°W), east (118°E), and south (175°E) (Irie et al., 2021; Mizobuchi et al., 2025). Each system consists mainly of a high-resolution ultraviolet–visible spectrometer (Maya2000Pro, Ocean Insight; 2048 detector channels, spectral resolution 0.2–0.4 nm), a telescope unit (manufactured by Prede Co., Ltd.), and optical fibers. Hyperspectral measurements obtained with this system are analyzed using our algorithm called the Japanese MAX-DOAS profile retrieval algorithm, version 2 (JM2) (Irie et al., 2011, 2015, 2019, 2021). JM2 simultaneously retrieves vertical profiles and tropospheric columns of eight components: NO_2, H_2O, formaldehyde, glyoxal, sulfur dioxide, ozone, and aerosol extinction coefficients at two wavelengths. Based on nearly two decades of experience with MAX-DOAS, we adopt elevation angles of 2°, 3°, 4°, 6°,

8°, and 70° as standard. Instead of 90°, 70° is used as the reference angle, which stabilizes the signal range across all elevation angles while maintaining constant spectrometer integration time. In the vertical profile retrieval, the elevation angle settings were fully accounted in the radiative transfer calculations used to compute the differential air mass factors (e.g., Irie et al., 2011, 2015, 2019). Low elevation angles are set below 10°, which minimizes potential systematic errors from oxygen collision complexes (O_4; O_2–O_2), reduces sensitivity to high-altitude retrievals (thus suppressing cloud interference), and enhances sensitivity to lower altitudes (Irie et al., 2015). Our unique MAX-DOAS observations are conducted within the framework of the international A-SKY ground-based remote sensing network (Irie et al., 2021) and are referred to as A-SKY/MAX-DOAS to distinguish them from other MAX-DOAS observations (e.g., Mizobuchi et al., 2025). To enhance the spatial representativeness around Chiba, which is located in an urban area, the average of the observations from these four azimuth directions was used in the analysis described below. Indeed, the obtained aerosol optical properties and trace gas concentration data have high spatial representativeness, extending several kilometers or longer in the horizontal direction, as recent studies by Damiani et al. (2021, 2022) showed a clear positive correlation between fine-mode aerosol absorption optical depth in the 0–1 km altitude range derived from these observations and black carbon (BC) mass concentrations measured using a Black Carbon Monitor (BCM3130; Kanomax Japan). BCM3130 was developed initially as Continuous Soot Monitoring System (COSMOS) by Miyazaki et al. (2008) and Kondo et al. (2009). The correlation ensures the spatial representativeness of the measured BC mass concentrations. At this well-characterized observation site, we conducted continuous measurements of CO_2 concentrations using trace gas analyzers of LI-7810 and G4301 together with A-SKY/MAX-DOAS.

3 Results and Discussion

Figures 2a and 2b show the time series of CO_2 concentrations measured using LI-7810 and G4301 at the Chiba University Atmospheric Environment Supersite in 2024. Hourly averages are plotted. As mentioned above, while the G4301 was calibrated with standard gases, the LI-7810 data are uncalibrated raw data. Nevertheless, both datasets exhibit variations between 420 and 600 ppmv, and within this relatively wide concentration range, both instruments exhibited approximately the same temporal variations. However, when their difference was analyzed, it was found that the difference varied gradually on a seasonal timescale (Fig. 2c). Over the course of 2024, the mean difference (± standard deviation) was −4.2 ± 4.2 ppmv. In addition, the differences spanned a relatively wide range from −16.9 to 26.5 ppmv. A pronounced difference of 26.5 ppmv occurred at 01:00 LT on December 3 (a day number of 338). At that time, the G4301 indicated 448.5 ppmv, whereas the LI-7810 measured 470.0 ppmv. The standard deviation of the 1-minute values within that hour was as high as 12.5 ppmv (~2.8%). This may have resulted from measuring a high-CO_2-concentration plume with relatively low spatial representativeness, particularly in urban atmospheres, due to imperfect coincidence of sampling location or timing. Thus, the complete removal of possible influence of an unexpected, highly localized emission source is challenging for monitoring of urban atmospheres.

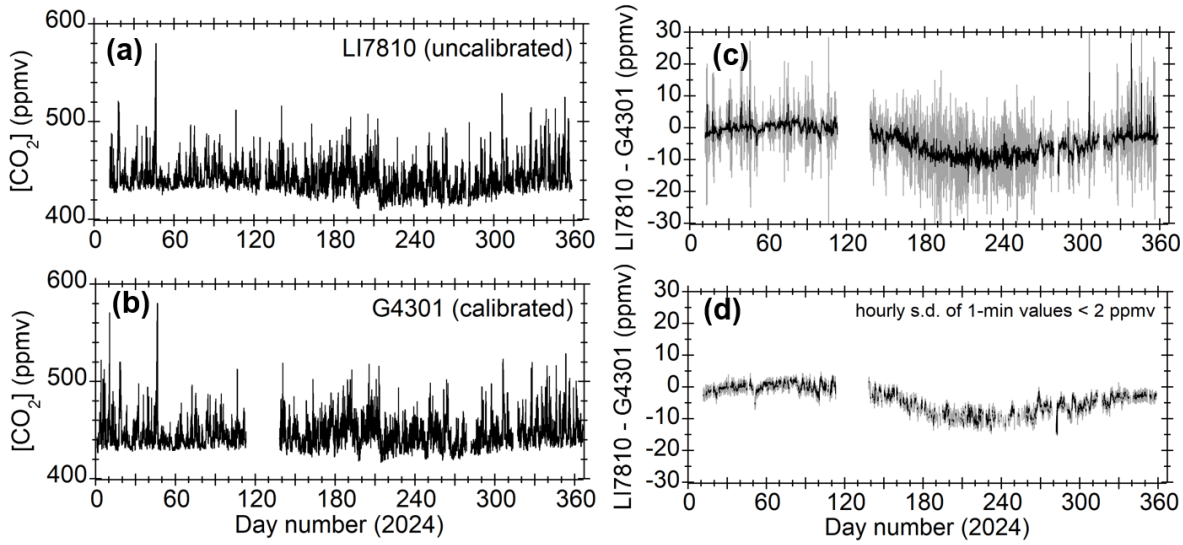

Figure 2: Time series plots of CO_2 concentrations measured using (a) G4301 and (b) LI-7810 the Chiba University Atmospheric Environment Supersite in 2024. Hourly averages are shown. Note that the G4301 was calibrated with standard gases and dehumidified, whereas the LI-7810 data are uncalibrated raw values. (c) Differences between LI-7810 and G4301 CO_2 concentrations. The gray shading indicates the 1σ standard deviation of the 1-minute values within each hour for LI-7810. (d) Differences between LI-7810 and G4301 CO_2 concentrations plotted only for hours in which the standard deviation was ≤ 2 ppmv.

To characterize these features further, a histogram of the standard deviations of the 1-minute values within each hour was examined for each of the LI-7810 and G4301 datasets (Fig. 3). The total numbers of hourly data points over the year were 8,092 and 7,036, respectively. Of these, nearly half had standard deviations of ≤ 2 ppmv. Conversely, the remaining half showed variations ≥ 2 ppmv, and in some cases exhibited very large fluctuations of up to ~30 ppmv. Based on these results, data with hourly standard deviations ≥ 2 ppmv were excluded to remove short-term large fluctuations (Fig. 2d), while it is difficult to uniquely determine the threshold. As a result, over the year 2024, the mean difference (± standard deviation) became −3.0 ± 3.6 ppmv, smaller than the mean before exclusion. Consequently, the gradual seasonal-scale variation in the differences between the two instruments became more clearly evident (Fig. 2d).

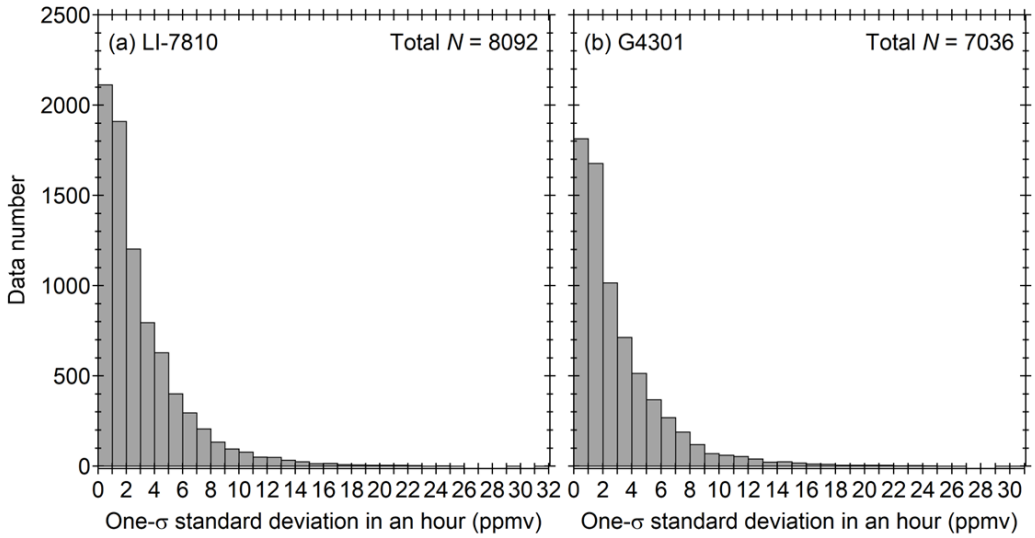

Figure 3: Histograms of the 1σ standard deviations of 1-minute CO_2 concentration data within each hour, measured by (a) LI-7810 and (b) G4301 at the Chiba University Atmospheric Environment Supersite in 2024. The total numbers of hourly data points of LI-7810 and G4301 for the year were 8,092 and 7,036, respectively.

To investigate the factors causing temporal variations on this seasonal scale, we examined the relationship with H_2O concentration data simultaneously derived with CO_2 and CH_4 by the LI-7810. Figure 4 shows not only the difference in CO_2 concentration measured by the LI-7810 and G4301, but also the time series of H_2O concentration derived concurrently with CO_2 by the LI-7810. As is immediately apparent, larger absolute differences in CO_2 concentration correspond to higher H_2O concentrations, indicating a significant negative bias in the uncalibrated LI-7810 data due to the interference by H_2O. It should be noted, however, that only data with a 1σ standard deviation of the 1-minute values within one hour less than 2 ppmv are plotted in Fig. 4. As the histogram (Fig. 3) shows, fluctuations exceeding 10 ppmv within an hour can occur regardless of H_2O concentration. In such cases, the relative importance of interference due to H_2O becomes smaller.

To quantitatively understand this relationship, their correlations were analyzed (Fig. 5). As expected, a clear anti-correlation was seen. From the slope of the regression line, we quantitatively estimated that a 1% increase in H_2O concentration corresponds to a negative bias of 3.6 ppmv in the CO_2 concentration. This regression line may be useful for applying a single bias-correction equation over the one-year period of 2024 and for analyses conducted on an annual timescale. However, it remains uncertain whether the H_2O interference introduces a bias in CO_2 concentration that consistently follows a linear relationship, and whether this works on seasonal timescales as well. In fact, although both the H_2O concentrations in January and December 2024 indicate approximately 0.5%, the CO_2 concentration differences between the LI-7810 and G4301 differ by several ppmv (Fig. 4). We also found that the two groups appeared in different seasons: one corresponding to the period from April to August when H_2O and temperature increase, and another corresponding to the period from September to December when they decrease. Comparing these groups, the slopes of the regression lines were similar, but the intercepts differed. The difference appears to be related to temperature and/or LI-7810 instrumental drift.

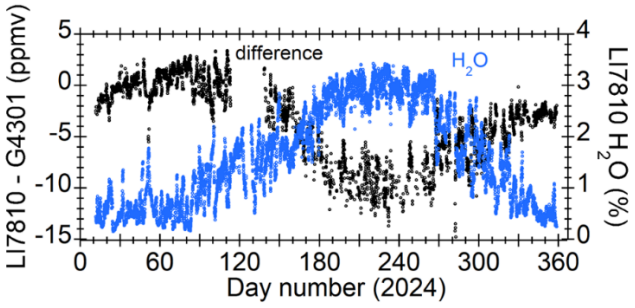

Figure 4: Time series of the difference in CO_2 concentration measured using the uncalibrated LI-7810 and the calibrated G4301 at the Chiba University Atmospheric Environment Supersite in 2024. Hourly averages are shown. Only differences for which the 1-hour standard deviation of the 1-minute data is ≤ 2 ppmv are plotted. The blue line indicates the time series of H_2O concentration simultaneously derived with CO_2 by the LI-7810.

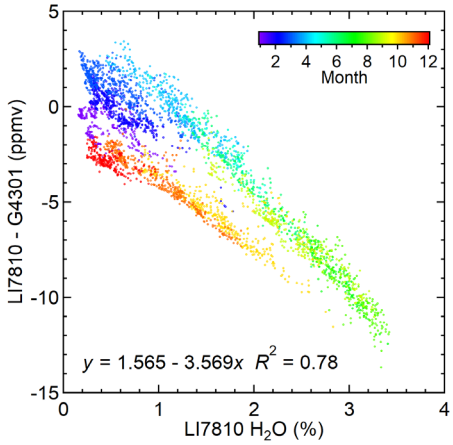

Figure 5: Correlations of the difference in CO_2 concentration measured using the uncalibrated LI-7810 and the calibrated G4301 with LI-7810 H_2O concentration data. Month is indicated by color. The regression line and its equation are also shown.

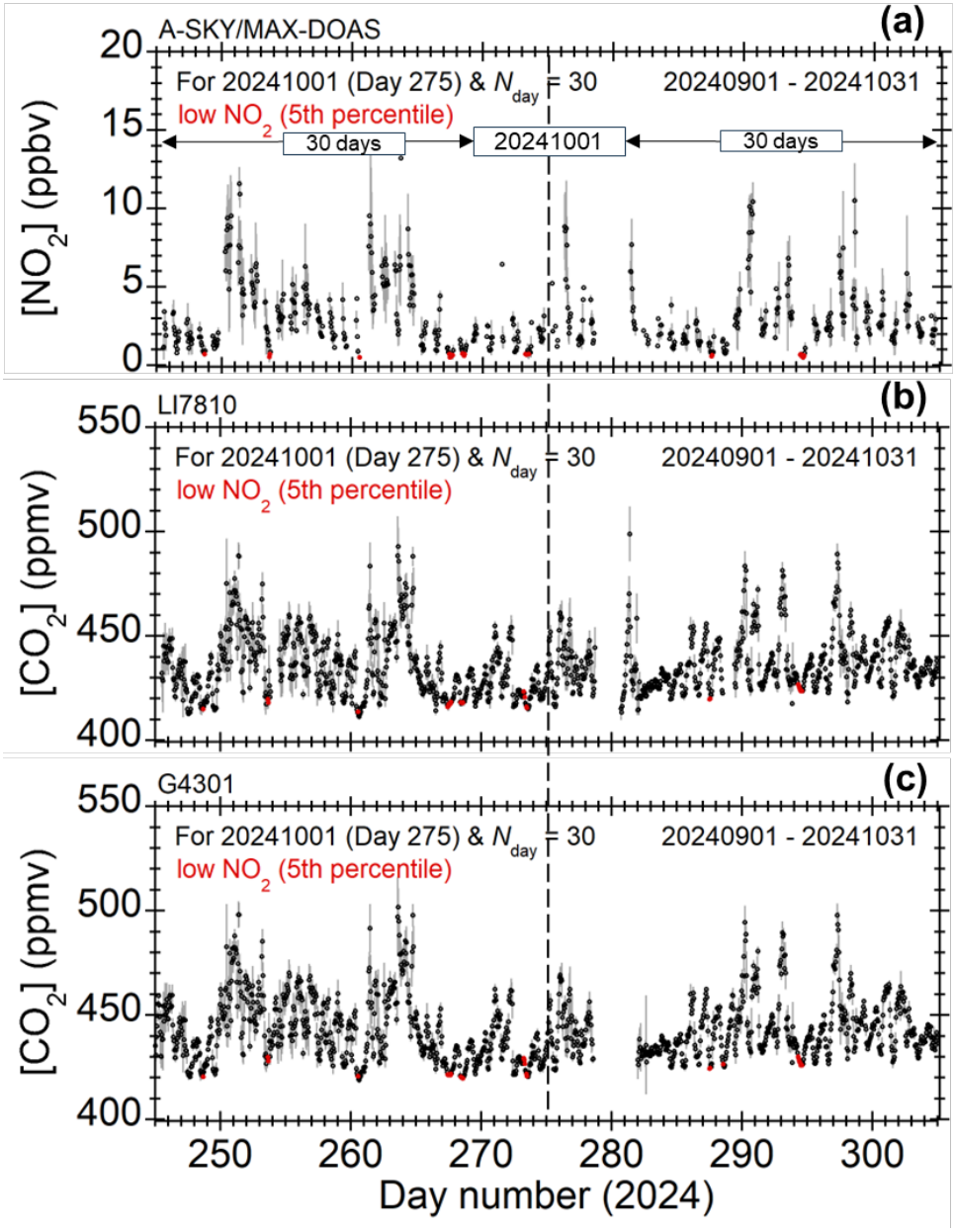

Figure 6: Time series of (a) NO_2 concentrations at 0–1 km altitude observed with A-SKY/MAX-DOAS and (b) LI-7810- and (c) G4301-measured CO_2 concentrations at the Chiba University Atmospheric Environment Monitoring Supersite from noon on September 1 to noon on October 31, 2024. Hourly averages are plotted. This period corresponds to ±30 days (N_{day} = 30) from noon on October 1, 2024. To estimate the expected CO_2 concentration $[CO_2^*]_N$ at noon on October 1, 2024 when NO_2 concentrations are not elevated, the 5th percentile of NO_2 data within the ±N day period was calculated. Values below the 5th percentile are shown in red in the panel a. The CO_2 concentration data measured at those identified times are shown in red in the panels b and c. For each of LI-7810 and G4301, the average of these CO_2 data was used to estimate $[CO_2^*]_N$ at noon on October 1, 2024.

Given these difficulties, an attempt was made to derive a baseline concentration ($[CO_2^*]_N$) by utilizing simultaneous A-SKY/MAX-DOAS observations of NO_2 concentration. Here, the brackets "[]" denote concentration. Figure 6a presents time series of NO_2 concentrations at 0–1 km altitude, retrieved from A-SKY/MAX-DOAS observations, together with CO_2 concentrations measured by LI-7810, covering the period from noon on September 1 to noon on October 31, 2024. This period corresponds to ±30 days (N_{day} = 30) from noon on October 1, 2024. To estimate the expected baseline CO_2

concentration $[CO_2^*]_N$ at noon on October 1, 2024 when NO_2 concentrations are not elevated, the 5th percentile of NO_2 data within the $\pm N_{day}$ period was calculated. Values below the 5th percentile are shown in red in Fig. 6a. The CO_2 concentration data measured at those identified times are shown in red in Figs. 6b and 6c. The average of these CO_2 data was used to estimate $[CO_2^*]_N$ at noon on October 1, 2024.

For the calibrated G4301, this $[CO_2^*]_N$ is considered to represent the CO_2 concentration determined by factors other than local influences (primarily advection to the site), and is expected to exhibit gradual temporal variations on a seasonal timescale. In contrast, for the uncalibrated LI-7810, in addition to seasonal variations, instrumental drift is also expected to contribute. Regarding this drift, the primary timescale to be removed is the gradual seasonal-scale variation indicated by the difference between LI-7810 and G4301. Therefore, in this estimation, N_{day} was set to 45 days, corresponding to half of three months. However, additional variations on timescales shorter than seasonal are also anticipated. To investigate this, $[CO_2^*]_N$ was also estimated with N_{day} set to 30 and 10 days.

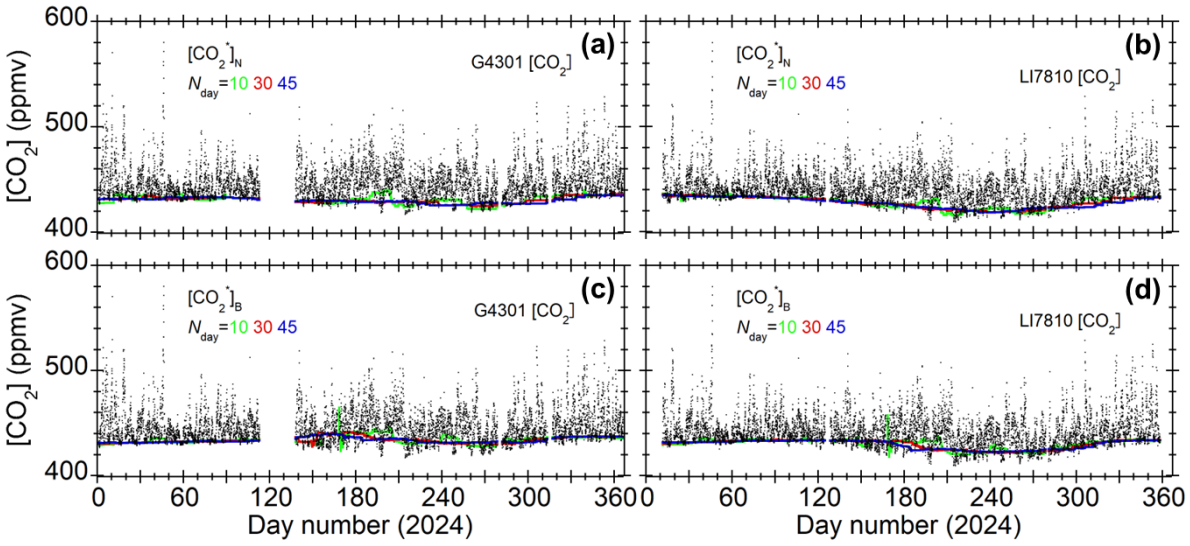

Figure 7: Time series of CO_2 concentrations ($[CO_2]$) measured using (a, c) G4301 and (b, d) LI-7810. One-hour averages are plotted. As described in the text, the G4301 data are calibrated with standard gases and dehumidified, whereas the LI-7810 data are uncorrected raw data. In panels a and b, the expected CO_2 concentration ($[CO_2^*]_N$) when NO_2 concentrations are not elevated is also shown, derived from simultaneous observations with A-SKY/MAX-DOAS. The green, red, and blue lines represent $[CO_2^*]_N$ estimated with N_{day} set to 10, 30, and 45, respectively. Panels c and d are similar, but show the expected CO_2 concentration when BC concentrations are not elevated ($[CO_2^*]_B$), based on simultaneous observations with COSMOS.

When N_{day} = 10 was used, $[CO_2^*]_N$ exhibited short-term fluctuations as well, likely due to insufficient number of data used for accurate estimations (Fig. 7). This suggested that an N_{day} longer than 10 days is more appropriate. On the other hand, comparison of $[CO_2^*]_N$ time variations with N_{day} set to 30 and 45 days showed that both produced similar gradual seasonal-scale changes. Thus, setting N_{day} to 30 days was found to be sufficient. This does not preclude the use of 45 days, but since shorter timescales can also be captured, a smaller N_{day} is preferable.

Similarly to $[CO_2^*]_N$, we also estimated $[CO_2^*]_B$, the expected CO_2 concentration during periods when BC concentrations measured simultaneously by COSMOS were notably low (Fig. 7). As shown, $[CO_2^*]_B$ also exhibited gradual seasonal-scale variations, supporting the $[CO_2^*]_N$ estimation. However, detailed analysis revealed that $[CO_2^*]_B$ was approximately 5 ppmv higher than $[CO_2^*]_N$. This indicates that CO_2 concentration increases can occur even when BC concentrations are very low. Such differences between $[CO_2^*]_B$ and $[CO_2^*]_N$ are interpreted, at least partly, by regulated BC emissions as a result of transitions such as from diesel to gasoline vehicles, or from coal-fired to natural gas-fired power generation.

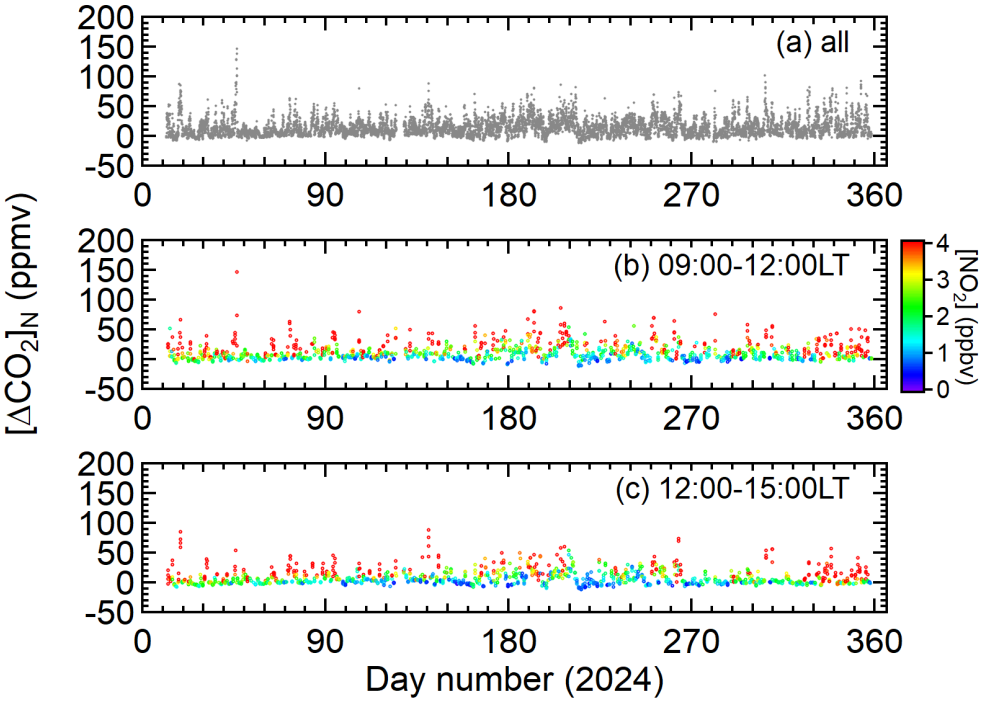

Figure 8: Time series of the CO_2 concentration increase ($[\Delta CO_2]_N$) obtained by combining LI-7810 and A-SKY/MAX-DOAS measurements. (a) All hourly values are plotted. To improve clarity by minimizing the influence of the diurnal variation pattern of NO_2, (b) the time series of $[\Delta CO_2]_N$ for local times of 09:00–12:00 and (c) for 12:00–15:00 are shown separately. The simultaneously measured NO_2 concentrations are indicated by color.

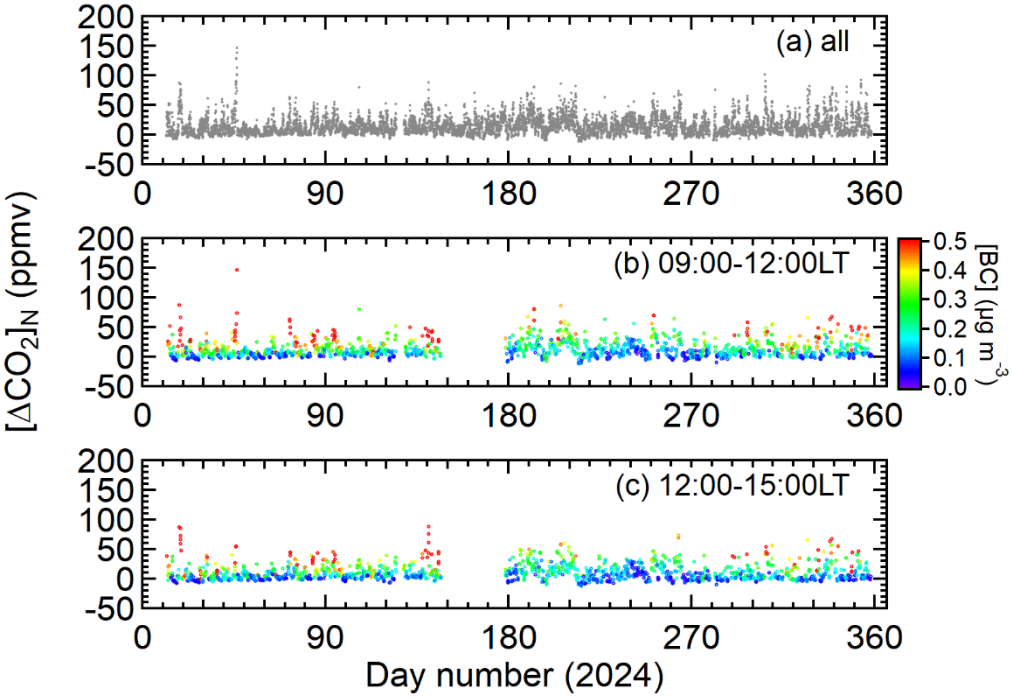

Figure 9: Same as Fig. 8 but BC concentrations are indicated by color.

Figure 8 shows a time series of the increase in CO_2 concentration $[\Delta CO_2]_N$, defined as $[CO_2]$ minus $[CO_2^*]_N$. The $[\Delta CO_2]_N$ values were obtained by combining LI-7810 and A-SKY/MAX-DOAS measurements. The estimated increase $[\Delta CO_2]_N$ reached 147 ± 2 ppmv at 09:00 on February 15 (Day 46). At this time, the A-SKY/MAX-DOAS NO_2 data reached 14 ± 4 ppbv, and the BC concentration also reached 1.9 ± 0.1 μg m^{-3}. As this example illustrates, the Figs. 8 and 9 clearly show that

when $[\Delta CO_2]_N$ is high, NO_2 and BC concentrations also tend to be elevated. The same features were also seen in the $[\Delta CO_2]_N$ values obtained by combining G4301 and A-SKY/MAX-DOAS (not shown to avoid redundancy).

To confirm the tendency, the correlation between $[\Delta CO_2]_N$ and $[NO_2]$ and the correlation between $[\Delta CO_2]_N$ and [BC] were analyzed (Fig. 10). Both exhibit clear positive correlations, indicating that the primary factors driving the increase in $[\Delta CO_2]_N$ are common with those responsible for increases in $[NO_2]$ and [BC]. In particular, the tight positive correlation with NO_2 (R^2 = 0.97 for LI-7810 and R^2 = 0.94 for G4301), which has a relatively short photochemical lifetime, suggests that the increase in $[\Delta CO_2]_N$ is mainly attributable to fossil-fuel combustion sources in the vicinity of the observation site. Thus, $[\Delta CO_2]_N$ observed in Chiba is considered to be closely linked to fossil-fuel CO_2 emissions in the urban atmosphere around Chiba, making it highly promising for monitoring purposes.

It should be noted that, in the present study, CO_2 enhancements were estimated by defining the baseline using NO_2, not by using the $[\Delta CO_2]_N$–$[NO_2]$ or $[\Delta CO_2]_N$–[BC] correlations. The slope of these correlations or the ratios (i.e., $[\Delta CO_2]_N/[NO_2]$ and $[\Delta CO_2]_N/$[BC]) may reflect differences in emission sources, meteorological conditions, photochemical processes, and the influence of vegetation. For example, air masses with a high $[\Delta CO_2]_N/[NO_2]$ ratio are likely associated with emissions from thermal power plants, whereas those with a low ratio are indicative of emissions from automobiles. Such detailed analyses, however, are beyond the scope of this study and will be investigated elsewhere. The regression line for the $[\Delta CO_2]_N$–$[NO_2]$ correlation shows an intercept close to zero (Fig. 10a), supporting the validity of the background concentration subtraction. Positive intercepts of the regression lines for the $[\Delta CO_2]_N$–[BC] correlations as seen in Fig. 10b are considered to have caused by regulated BC emissions as a result of transitions such as from diesel to gasoline vehicles, or from coal-fired to natural gas-fired power generation, as mentioned earlier. The data point with the highest BC concentration may have influenced the intercept of the regression line. To assess this effect, we excluded the highest-BC data point and found that the intercept remained positive, although it decreased from ~5 to ~2 ppmv.

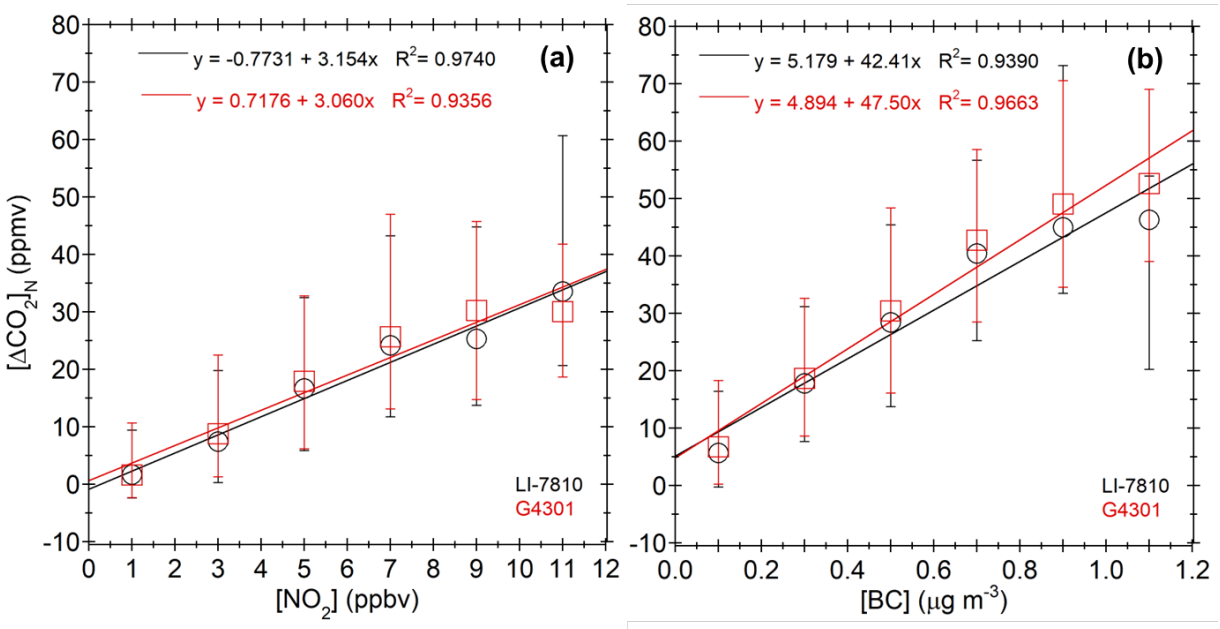

Figure 10: (a) Correlation between $[\Delta CO_2]_N$ and A-SKY/MAX-DOAS NO_2 data. (b) Correlation between $[\Delta CO_2]_N$ and COSMOS BC data. In each plot, the median values are shown for bins of 2 ppbv (for NO_2) and 0.2 μg m^{-3} (for BC). LI-7810 and G4301 data are shown in black and red, respectively. Error bars represent the range encompassing 67% of the data points.

To evaluate the accuracy and precision of the $[\Delta CO_2]_N$ estimate, we examined the correlation of $[\Delta CO_2]_N$ values derived from CO_2 measurements with LI-7810 and G4301 (Fig. 11). As shown in the figure, the regression line of this correlation exhibited a very high coefficient of determination (R^2 = 0.98), a slope close to unity (0.97), and an intercept nearly equal to

zero (-0.90 ppmv). It should be noted that the LI-7810 observations were conducted without performing regular calibrations and without dehumidifying the sampled air. Nevertheless, the $[\Delta CO_2]_N$ values obtained from both instruments agreed remarkably well. This indicates that simultaneous measurements of CO_2 with A-SKY/MAX-DOAS NO_2 enable highly accurate and precise estimation of $[\Delta CO_2]_N$.

Another noteworthy aspect concerns the error analysis. Figure 11 also shows error bars representing the uncertainty of $[\Delta CO_2]_N$. The uncertainty is considered to originate from 1) hourly fluctuations in CO_2 concentration, 2) the magnitude of variability in CO_2 values measured when the NO_2 concentration was below its 5th percentile, and 3) drift on time scales shorter than N_{day} (including interference effects of water vapor). Despite these characteristics, $[\Delta CO_2]_N$ values derived from LI-7810 and G4301 both exhibited nearly the same magnitude of error (Fig. 11). Although the error in LI-7810 $[\Delta CO_2]_N$ due to the drift was evidently larger than that of G4301, the overall error magnitude was nearly identical, suggesting that the contribution of the drift was relatively small, and that the other factors 1 and 2 were the dominant sources of uncertainty. This is also supported by the fact that the mean difference (± 1σ standard deviation) between LI-7810 $[\Delta CO_2]_N$ and G4301 $[\Delta CO_2]_N$ was -1.3 ± 2.1 ppmv, which is very small, and the mean error was within the range of the 1σ standard deviation. Thus, even when CO_2 measurements from an uncalibrated gas analyzer were used, we found that simultaneous measurements with NO_2 provide a simple and accurate means of monitoring fossil-fuel combustion-derived CO_2 concentrations in the Greater Tokyo Area.

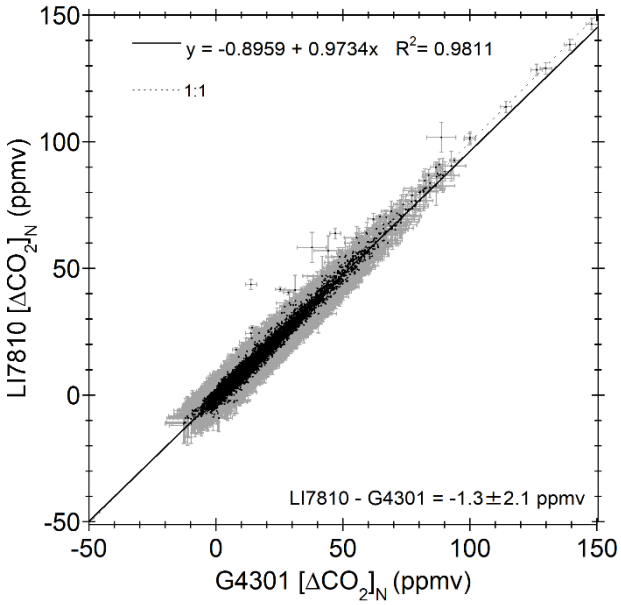

Figure 11: Correlation between $[\Delta CO_2]_N$ values estimated from LI-7810 and G4301 CO_2 data using simultaneous A-SKY/MAX-DOAS NO_2 observations. Hourly values are plotted. Gray error bars indicate the uncertainty in $[\Delta CO_2]_N$. The uncertainty is considered to include 1) hourly fluctuations in CO_2 concentration, 2) the uncertainty in estimating $[CO_2^*]_N$, and (3) drift on time scales shorter than N_{day} (including interference effects of water vapor). The 1:1 relationship is shown by the dotted line.

4 Conclusions

To clarify the usefulness of simultaneous near-surface CO_2 and NO_2 measurements for simple and accurate monitoring of fossil-fuel combustion-derived CO_2 in the Greater Tokyo Area, year-round continuous measurements of near-surface CO_2 concentrations using LI-7810 and G4301 trace gas analyzers were conducted simultaneously with NO_2 measurements by A-SKY/MAX-DOAS at Chiba, located within the Greater Tokyo Area, during 2024. These simultaneous measurements revealed that CO_2 concentrations were low on days when near-surface NO_2 concentrations were also low. Furthermore, the $[\Delta CO_2]_N$ values estimated based on such low-NO_2-concentration days was positively correlated with NO_2 and BC

concentrations. This finding indicates that $[\Delta CO_2]_N$ captures the increase in fossil-fuel combustion-derived CO_2 within the Greater Tokyo Area. Interestingly, the correlation of $[\Delta CO_2]_N$ values derived from LI-7810 and G4301 showed a very high coefficient of determination (R^2 = 0.98), a slope close to unity (0.97), and an intercept nearly equal to zero (-0.90 ppmv), although the LI-7810 observations were conducted without performing regular calibrations and without dehumidifying the sampled air. By employing this relatively simple method, fossil-fuel combustion-derived CO_2 concentrations in megacities such as the Greater Tokyo Area can be monitored with high accuracy and precision, contributing to more effective emission mitigation strategies.

Code, data, or code and data availability

The LI-7810 and MAX-DOAS data are available upon request to the corresponding author (hitoshi.irie@chiba-u.jp). The G4301 data are available upon request to Yukio Terao (yterao@nies.go.jp).

Author contributions

HI, MN, and YK designed the present study, performed observation and analysis, and wrote the paper, with support from all the authors. YT performed the G4301 measurement and participated in the discussion of results. All authors have read and agreed to the published version of the manuscript.

Competing interests

The authors declare that they have no competing interest.

Acknowledgements

We thank Ms. Miho Ohama and Ms. Megumi Uehara for their technical assistance in the continuous operation of the instruments. The measurements using G4301 were supported by Dr. Toshinobu Machida and Dr. Motoki Sasakawa for the NIES09 CO_2 scale. We acknowledge the free use of TROPOMI tropospheric NO_2 column data from www.temis.nl.

Financial support

This research was supported by JSPS KAKENHI (grant numbers 20H04320 and 22H05004), the JAXA 4th research announcement on the Earth Observations, and the Virtual Laboratory (VL) project by the Ministry of Education, Culture, Sports, Science and Technology (MEXT), Japan. The measurements using G4301 were supported by the Environment Research and Technology Development Fund (JPMEERF21S20810 and JPMEERF24S12202) of the Environmental Restoration and Conservation Agency, provided by the Ministry of the Environment of Japan.

References

Bisht, J. S. H., Patra, P. K., Takigawa, M., Kanaya, Y., Yamaguchi, M., Machida, T., and Tanimoto, H.: High-resolution simulation of CO_2 using WRF-GHG over the Kanto region in Japan, Journal of Geophysical Research: Atmospheres, 130, e2025JD043589, https://doi.org/10.1029/2025JD043589, 2025.

Damiani, A., Irie, H, Belikov, D. A., Kaizuka, S., Hoque, H. M. S., and Cordero, R. R.: Peculiar COVID-19 effects in the Greater Tokyo Area revealed by spatiotemporal variabilities of tropospheric gases and light-absorbing aerosols, Atmos. Chem. Phys., 22, 12705–12726, https://doi.org/10.5194/acp-22-12705-2022, 2022.

Damiani, A., Irie, H., Yamaguchi, K., Hoque, H. M. S., Nakayama, T., Matsumi, Y., Kondo, T., and Da Silva, A.: Variabilities in $PM_{2.5}$ and black carbon surface concentrations reproduced by aerosol optical properties estimated by sky radiometer and MAX-DOAS instruments, Remote Sensing, 13(16), 3163, https://doi.org/10.3390/rs13163163, 2021.

Hirano, T., Sugawara, H., Murayama, S., and Kondo, H.: Diurnal variation of CO_2 flux in an urban area of Tokyo. SOLA, 11, 100–103, https://doi.org/10.2151/sola.2015-024, 2015.

IPCC (Intergovernmental Panel on Climate Change): Climate Change 2021: The Physical Science Basis, Cambridge University Press, Cambridge, 2021.

Irie, H., Kanaya, Y., Akimoto, H., Iwabuchi, H., Shimizu, A., and Aoki, K.: First retrieval of tropospheric aerosol profiles using MAX-DOAS and comparison with lidar and sky radiometer measurements, Atmospheric Chemistry and Physics, 8, 341-350, https://doi.org/10.5194/acp-8-341-2008, 2008.

Irie, H., Takashima, H., Kanaya, Y., Boersma, K. F., Gast, L., Wittrock, F., Brunner, D., Zhou, Y., and Van Roozendael, M.: Eight-component retrievals from ground-based MAX-DOAS observations, Atmospheric Measurement Techniques, 4, 1027-1044, https://doi.org/10.5194/amt-4-1027-2011, 2011.

Irie, H., Nakayama, T., Shimizu, A., Yamazaki, A., Nagai, T., Uchiyama, A., Zaizen, Y., Kagamitani, S., and Matsumi, Y.: Evaluation of MAX-DOAS aerosol retrievals by coincident observations using CRDS, lidar, and sky radiometer in Tsukuba, Japan, Atmospheric Measurement Techniques, 8, 2775-2788, doi:10.5194/amt-8-2775-2015, 2015.

Irie, H., Yonekawa, D., Damiani, A., Hoque, H. M. S., Sudo, K., and Itahashi, S.: Continuous multi-component MAX-DOAS observations for the planetary boundary layer ozone variation analysis at Chiba and Tsukuba, Japan from 2013 to 2019, Progress in Earth and Planetary Science, 8, 31, https://doi.org/10.1186/s40645-021-00424-9, 2021.

Irie, H., International air quality and sky research remote sensing network (A-SKY): Its development and satellite atmosphere product validation, Journal of the Remote Sensing Society of Japan, 41, 5, 575-581, https://doi.org/10.11440/rssj.41.575, 2021.

Irie, H., and Nakajima, T.: SKYNET, In: Akimoto H., Tanimoto H. (eds) Handbook of Air Quality and Climate Change, Springer Nature, Singapore, https://doi.org/10.1007/978-981-15-2527-8_52-1, 2022.

Kondo, Y., Sahu, L., Kuwata, M., Miyazaki, Y., Takegawa, N., Moteki, N., Imaru, J., Han, S., Nakayama, T., Kim Oanh, N. T., Hu, M., Kim, Y. J., and Kita, K.: Stabilization of the mass absorption cross section of black carbon for filter-based absorption photometry by the use of a heated inlet. Aerosol Sci. Technol., 43, 741–756, https://doi.org/10.1080/02786820902889879, 2009.

Li, J., Li, P., Han, P., Cheng, Z., Li, J., Zhang, T., Chen, D., Zheng, Y., Zeng, N., and Zhang, G.: Advances in the design of urban CO_2 emission monitoring networks: a review, Carbon Research, 5, 3, https://doi.org/10.1007/s44246-025-00239-z, 2026.

Long, Y., and Yoshida, Y.: Quantifying city-scale emission responsibility based on input-output analysis – insight from Tokyo, Japan, Appl. Energy, 218, 349–360, 2018.

Miyazaki, Y., Kondo, Y., Sahu, L. K., Imaru, J., Fukushima, N., and Kano, M.: Performance of a newly designed continuous soot monitoring system (COSMOS). J. Environ. Monit. 10, 1109–1240, https://doi.org/10.1039/B806957C, 2008.

Mizobuchi, S., Irie, H., and Shimizu, S.: Long-term continuous observations of horizontal inhomogeneity in water vapor concentration in the lower atmosphere using A-SKY/MAX-DOAS, Progress in Earth and Planetary Science, 12, 52, https://doi.org/10.1186/s40645-025-00724-4, 2025.

Morville, J., Romanini, D., and Kerstel, E.: Cavity Enhanced Absorption Spectroscopy with Optical Feedback, in: Cavity-Enhanced Spectroscopy and Sensing, Vol. 179, edited by: Gagliardi, G. and Loock, H.-P., Springer Berlin Heidelberg, Berlin, Heidelberg, 163–209, https://doi.org/10.1007/978-3-642-40003-2_5, 2014.

Nakajima, T., Campanelli, M., Che, H., Estellés, V., Irie, H., Kim, S. W., Kim, J., Liu, D., Nishizawa, T., Pandithurai, G., Soni, V. K., Thana, B., Tugjsurn, N. U., Aoki, K., Go, S., Hashimoto, M., Higurashi, A., Kazadzis, S., Khatri, P., Kouremeti,

N., Kudo, R., Marenco, F., Momoi, M., Ningombam, S. S., Ryder, C. L., Uchiyama, A., and Yamazaki, A.: An overview of and issues with sky radiometer technology and SKYNET, Atmos. Meas. Tech., 13, 4195–4218, 2020.

Pisso, I., Patra, P., Takigawa, M., Machida, T., Matsueda, H., and Sawa, Y.: Assessing Lagrangian inverse modelling of urban anthropogenic CO_2 fluxes using in situ aircraft and ground-based measurements in the Tokyo area, Carbon Balance Manage, 14, 6, https://doi.org/10.1186/s13021-019-0118-8, 2019.

Romanini, D., Ventrillard, I., Méjean, G., Morville, J., and Kerstel, E.: Introduction to Cavity Enhanced Absorption Spectroscopy, in: Cavity-Enhanced Spectroscopy and Sensing, Vol. 179, edited by: Gagliardi, G. and Loock, H.-P., Springer Berlin Heidelberg, Berlin, Heidelberg, 1–60, https://doi.org/10.1007/978-3-642-40003-2_1, 2014.

Shirai, T., Machida, T., Matsueda, H., Sawa, Y., Niwa, Y., Maksyutov, S., and Higuchi, K.: Relative contribution of transport/surface flux to the seasonal vertical synoptic CO_2 variability in the troposphere over Narita, Tellus B, 64, 19138, doi:10.3402/tellusb.v64i0.19138, 2012.

Sugawara, H., Ishidoya, S., Terao, Y., Takane, Y., Kikegawa, Y., and Nakajima, K.: Anthropogenic CO_2 emissions changes in an urban area of Tokyo, Japan, due to the COVID-19 pandemic: A case study during the state of emergency in April–May 2020, Geophysical Research Letters, 48, e2021GL092600. https://doi.org/10.1029/2021GL092600, 2021.

UNDP (United Nations Population Division): The World's cities in 2018: data booklet. The 2018 Revision Rep., United Nations., 2018.

Verhoelst, T., Compernolle, S., Pinardi, G., Lambert, J.-C., Eskes, H. J., Eichmann, K.-U., Fjæraa, A. M., Granville, J., Niemeijer, S., Cede, A., Tiefengraber, M., Hendrick, F., Pazmiño, A., Bais, A., Bazureau, A., Boersma, K. F., Bognar, K., Dehn, A., Donner, S., Elokhov, A., Gebetsberger, M., Goutail, F., Grutter de la Mora, M., Gruzdev, A., Gratsea, M., Hansen, G. H., Irie, H., Jepsen, N., Kanaya, Y., Karagkiozidis, D., Kivi, R., Kreher, K., Levelt, P. F., Liu, C., Müller, M., Navarro Comas, M., Piters, A. J. M., Pommereau, J.-P., Portafaix, T., Prados-Roman, C., Puentedura, O., Querel, R., Remmers, J., Richter, A., Rimmer, J., Rivera Cárdenas, C., Saavedra de Miguel, L., Sinyakov, V. P., Stremme, W., Strong, K., Van Roozendael, M., Veefkind, J. P., Wagner, T., Wittrock, F., Yela González, M., and Zehner, C.: Ground-based validation of the Copernicus Sentinel-5P TROPOMI NO_2 measurements with the NDACC ZSL-DOAS, MAX-DOAS and Pandonia global networks, Atmos. Meas. Tech., 14, 481–510, https://doi.org/10.5194/amt-14-481-2021, 2021.

Yamada, K., Niwa, Y., Terao, Y., Tohjima, Y., Tsuboi, K., Ishijima, K., and Murayama, S.: Estimation of CO_2 fluxes from Tokyo using a global model and tower observation, J. Meteor. Soc. Japan, 103, 67–85, doi: 10.2151/jmsj.2025-004, 2025.